Gamma ray Imaging Based Methods to Improve the Accuracy of Uranium Holdup Quantification

[1]Ramkumar Venkataraman, [1]Klaus-Peter Ziock, [1]Matthew Blackston, [1]Angela Lousteau, [1]Stephen Croft, [1]Keith Bledsoe, [1]Jordan Lefebvre

[1]Oak Ridge National Laboratory
PO Box 2008, MS-6166, Oak Ridge, TN 37831-6166

[2]Jeff Preston and [2]Justin Knowles

[2]Y-12 National Security Complex
Oak Ridge, TN

ABSTRACT

Deposits in commercial uranium processing facilities of interest to nuclear safeguards are predominantly low enriched uranium (LEU). The shapes and sizes of holdup deposits can vary significantly, thus making it difficult to model the deposits accurately for calibration purposes. This presents a challenge to currently employed methods such as the Generalized Geometry Holdup (GGH) that rely on quantifying ^{235}U mass by simplifying deposit shapes as a point, a line, or an area. In this work, gamma ray imaging using high energy resolution Germanium Gamma Imagers (GeGI™) is employed to determine the distribution of uranium inside the source containment. Two types of imaging methods are employed; coded-aperture imaging and Compton imaging. Gamma-ray emissions seen in different regions of the image are quantified using an inverse gamma-ray transport solver being developed at ORNL. Using measured data, the inverse method will be used to solve for unknown source parameters such as source matrix thickness, density, and attenuation due to container wall and shielding. The intrinsic efficiency of the detector is determined based on a library of built-in response functions and key dimensions of the detector (e.g., thickness and radius of the detector crystal). Measurements are performed in both imaging modalities using uranium sources of well-known masses and enrichments configured inside mocked-up holdup fixtures. Results from the two imaging modalities are intercompared. The paper presents preliminary results of the imaging measurements and the progress made in the computational methods to quantify uranium mass.

Keywords: Holdup; Gamma-ray Imaging, Coded aperture, Compton imaging, Markov Chain Monte-Carlo

1. Introduction

Holdup is the residual special nuclear material (SNM) remaining in a processing facility after production materials are removed or accounted for. Material holdup in commercial uranium processing facilities, currently operational as well as facilities undergoing decommissioning, is predominantly low enriched uranium (LEU). Accurate estimation of uranium holdup in process equipment is important from an international safeguards perspective as well as domestic nuclear material accounting and control (NMAC). The shapes and sizes of holdup deposits can vary significantly, making it difficult for current holdup approaches to accurately determine the amount of material present. For instance, the widely used Generalized Geometry Holdup (GGH) method attempts to reign in the complexity of deposit shapes by simplifying them for single measurements as either a point, a line, or an area[1],[2].While the GGH methodology provides acceptable results, it is labor intensive, and based on comparison to recovery, the corresponding uncertainties can be ±50% or higher.. It is important to reduce such large uncertainties as they reduce the material unaccounted for (MUF), consequently mitigating the threat of material diversion, theft, and facility misuse. In a traditional gamma spectrometry analysis, radionuclide activity or mass is quantified using: (i) the net peak count rate in the Full Energy Peak (FEP) (also known as photopeak), typically based on a two-region-of-interest algorithm to extract the 186-keV feature intensity. It also uses the geometrical efficiency of the detector (that corrects for solid angle and source-to-detector distance), intrinsic efficiency of the detector, and corrections for self-attenuation, and attenuation through any intervening absorbers between the source and the detector.

The GGH approach has to date been the predominant means of quantifying highly enriched uranium holdup whereas, our focus is on LEU. In this application the signal strength is lower and self-attenuation may be more severe due to larger deposit thicknesses. This means that the GGH approach, as historically practiced using the HMS-4 system, is sub-optimal for LEU. This research is part of an effort to look at alternative, modern, robust, flexible, cost effective strategies.

Specifically, we are exploring the use of gamma-ray imaging technologies with high spectral resolution to delineate the shape of the holdup deposits while also capturing the activity variations in distributed sources. The combination of imaging and high spectral resolution eliminate interferences and confounding factors. Further, the hyperspectral images created have a spectrum for each pixel of the image opening up the possibility of applying attenuation corrections on a pixel-by-pixel basis. In addition, each image is made over a wider area with the instrument left to integrate the data, potentially reducing manpower and worker radiation exposure. Combining Compton and coded-aperture imaging allows us to effectively use both the 186 keV (present in both HEU and LEU) and the more penetrating 1001 keV radiation (predominately present in LEU).

In this work, count data from the image pixels of a source distribution are used to solve for uranium source strength. The intrinsic efficiency of the detector (GeGI^{TM}) and its enclosure is determined using a measurement validated GEANT4[3] Monte-Carlo model. A mathematically rigorous Differential Evolution Adaptive Metropolis (DREAM), a Markov Chain Monte-Carlo transport method[4],[5],[6] is employed to determine attenuation characteristics of source and overlying materials. The source-to-detector

geometry corrections are made on a pixel-by-pixel basis. The DREAM code also provides rigorous uncertainty quantification from the measured data to the solution.

2. Uranium source measurements using GeGI™

The imagers are based on a position-sensitive GeGI™ detector (Figure 1), manufactured by PHDS Company, comprising a mechanically cooled high purity germanium (HPGe) detector in a hand-held form factor. The planar Ge (1 cm thick, ~ 9 cm diameter) -detector in the instrument uses a crossed-strip electrode design with 16 anodes and cathodes, both with a 5 mm pitch. The 32-channel readout system records the signals from the collected charge (electrons and holes) on the strips on opposite faces of the detector to provide energy and coarse (5-mm) localization. It also records the transient signals seen on adjacent strips and uses these to interpolate the lateral event locations (~ 1 mm). Finally, the system records the charge carrier arrival times at the opposite faces, and uses these to determine the depth of interaction of each event (~ 1 mm). The combined result allows for high fidelity localization of radiation events within the detector, enabling a very large number of voxels that act as logical detectors for Compton imaging. The detector can also be mated with a coded-aperture shadow mask[6] as an alternate imaging modality. In addition to on-line image generation for both imaging modalities, the data can be saved as list-mode data files for more refined analysis off-line.

Uranium sources of known masses and enrichments available at ORNL were measured with GeGI™ spectrometers, using coded aperture[7] and Compton imaging[8]. The two imaging modalities are complementary with respect to the photon energy regimes where the response is the highest. For coded-aperture imaging, the performance falls off above 300 keV. This is because the technique relies on detecting the full energy peak (photopeak) emission from the source. So, the signal from prominent direct gamma ray emissions from ^{235}U, namely 143 keV, 163 keV, 186 keV, and 205 keV are well suited for coded-aperture imaging. Conversely, Compton imaging requires two-site interactions in the detector, a scatter event followed by photo-absorption, so it is more effective at higher energies such as the gamma emissions from ^{234m}Pa, the grand-daughter of ^{238}U, at energies of 766 keV and 1001 keV.

Coded-aperture imaging[9] (Figure 2) uses a shadow mask (50% open area) placed between the scene and a position-sensitive detector to encode the scene onto the detector. The image of the scene is reconstructed by using cross-correlation of the known mask pattern with the shadow pattern measured by the detector[10]. The mask is made of a 4-fold repetition of a base pattern that is nominally the same

size as the detector. The portion of the mask that is projected onto the detector depends on the source location. Different detector-sized regions of the mask are both unique and produce “orthogonal” shadow patterns so that a complex source field can be imaged. The technique encodes the scene as spatial variations in counts across the detector so any count rate variations across its face will appear in the reconstructed image. Inevitably residual detector non-linearities and non-uniform background event rates will occur and these produce artifacts in an image. However, these can be almost completely eliminated if the data are collected in two equal-time integrations, one with the mask and the second with its inverse, or anti-mask. In the anti-mask, the open and closed pixels of the pattern are interchanged with those of the mask so that each integration interval effectively measures the foreground plus background with half of the detector, and the background with the other half. The backgrounds can be subtracted before the image reconstruction. The mask/anti-mask exchange is made autonomously by the instrument by taking advantage of the fact that the modified uniformly redundant array mask pattern[6] used in the imager is anti-symmetric when rotated through 90 degrees.

Figure 2. GeGI™ with ORNL coded aperture mask

Compton Imaging is an application of the fundamental photon interaction of Compton scattering where a gamma-ray scatters elastically off of a (free) electron in the detector. Conservation of energy and momentum for the event allows one to calculate the angle through which the gamma-ray scatters using the measured energy imparted to the electron and that of the initial gamma-ray. The latter is determined by adding the electron energy to a second interaction in the detector that records the energy of the scattered gamma-ray. The location of the two sites determines the direction to which the gamma ray scattered so that the direction of incidence of the gamma ray can be restricted to a cone of directions defined by the calculated scatter angle (the redundancy occurs because the scatter direction of the electron is not known.) An image of a point source is created when the cones determined for multiple gamma-rays from the source intersect. (In the far field, the cones are projected as circles.)

The holdup mock-up fixtures available at the Safeguards Laboratory at ORNL were used as structural models for holdup scenarios. Uranium oxide (U_3O_8) sources (93% enrichment, ~ 11 g ^{235}U) available in the form factor of cards (46 cm x 23 cm, length x width) were measured bare, and then configured inside an L-duct fixture (Figure 3) and a round duct fixture (Figure 4) to mock-up fissionable deposits inside process equipment. Even though the card sources are highly enriched uranium, they provide a good starting point to benchmark the gamma imaging approaches.

Figure 3. L-Duct Holdup Mock-up Fixture

Figure 4. Round Duct Holdup Mock-up Fixture

2.1 Gamma ray images from coded aperture imaging

The gamma ray images taken from a distance of 106 cm for card source #10, bare, inside the L-Duct, and inside the round duct are shown in Figures five, six, and seven, respectively. The simultaneous image for card sources #1 and #10, inside the L-duct are shown in Figure 8. The images show the total collected data for each configuration; 15 hours for the bare card, 3.5 hours for the card in the L-Duct, and 36 hours for the card in the round duct. The objective was to acquire data with excellent counting statistics so that the imaging results could be benchmarked. The data were acquired in alternating 900 s intervals using the mask and anti-mask configurations. From the list mode data files that were collected images for shorter integrations of any duration can be generated to evaluate the impact of poorer counting statistics on the image quality, and the quantification accuracy. Operationally there may be scenarios where long counts are acceptable. We have in mind cases where an instrument can be setup and left unattended, allowing a large area to be scanned while minimizing human exposure to harsh physical conditions.

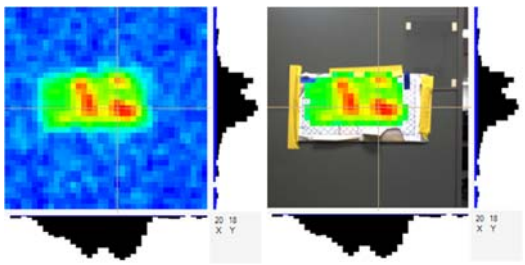

Figure 5. Card source #10 (bare)

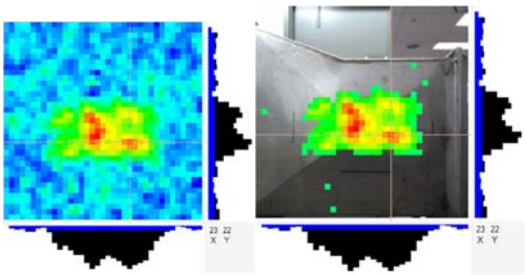

Figure 6. Card source #10 inside L-Duct

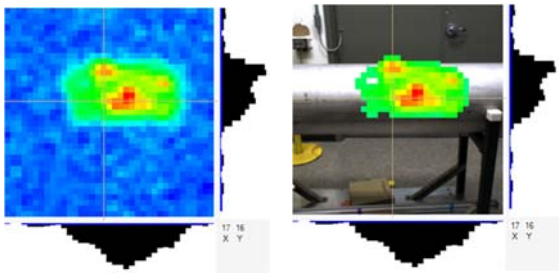

Figure 7. Card source #10 inside Round duct

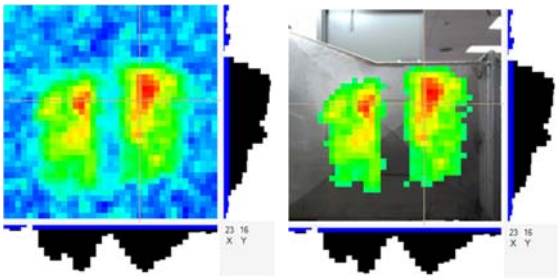

Figure 8. Card sources #1 and #10 inside L-Duct

In each of the figures, the image on the left shows the false-color gamma-ray image, while the figure on the right shows the same gamma-ray image overlaid on a visible-light image of the same scene. The gamma-ray intensity increases from blue to red and is scaled independently for each image. In the overlay image gamma-ray pixels below a given threshold (typically 50%) are turned clear to allow localizing the gamma-ray emissions. The histograms below and to the right of the images show the counts in each of the pixels under the horizontal and vertical tan cursor lines, respectively. Close inspection reveals the histograms include both and blue and black portions, with the transition from blue to black representing zero counts. The images were made using only counts in the 186-keV photopeak. Figure 8 shows that the images of the two cards, #1 and #10, are well separated.

Quantitative analysis of the bare card data using the known imager response and the distance to the source is in progress. Results from summing the counts in each of the image pixels gives estimates for the ^{235}U mass that scatter about an average for the different cards by only a few percent. The results obtained for the four bare cards are slightly low, ranging from 1.1 to 3 % below the known material mass. Some of this discrepancy can be linked to the fact that we are not currently including material self-attenuation effects. However, we are still exploring other subtle instrumental effects that could be at the percent level.

2,2 Compton Imaging of Uranium Card Sources

The Compton gamma-ray images for card source ID#10, both bare and inside the L-Duct, are shown in Figure 9 and 10, respectively. Both images represent 1 hour of data collected from a distance of 96.5 cm. Using the vendor software, with the “Width” parameter is set to 10%, gamma lines were imaged simultaneously for 185.7 keV, 163.4 keV, 205.3 keV, and 194.5 keV, however the 238.6-keV and 583.2-keV lines did not have sufficient statistics to obtain adequate results within the allotted time.

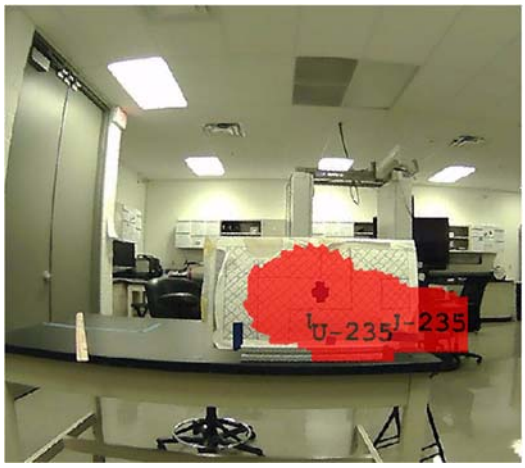

Figure 9. Compton Image of Card #10 (Bare)

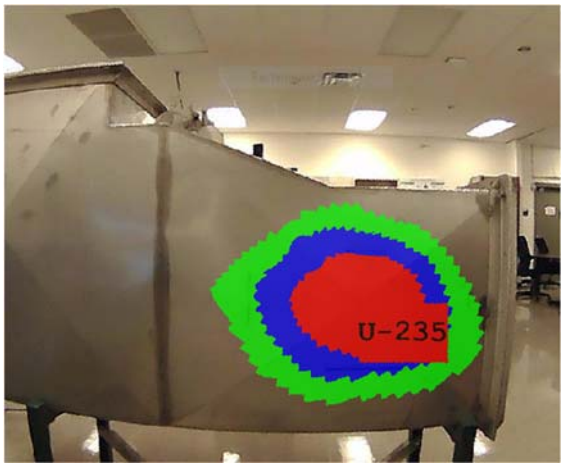

Figure 10. Compton Image of Card #10 (inside L-Duct)

3. Intrinsic Efficiency of GeGI™ based on GEANT4 Model

Deriving accurate quantitative results from images requires good knowledge of the imaging efficiencies for the instrument being used. For the coded-aperture technique, fewer counts are expected when detector pixels are behind closed elements of the mask. If detector pixels or rows of pixels have reduced intrinsic efficiencies relative to other pixels, then these variations can mimic or obscure the effects of the shadow cast by the mask, altering the quantitative values of pixels in the reconstructed image. For the GeGI™ detector, reductions in detection efficiency near the boundaries between strips can be severe, impacting the imaged results. In order to determine how systematic effects impact the efficiencies for the GeGI™ detector, a model of the detector was created using the Monte Carlo radiation transport code GEANT4[9] and a response model was developed to convert simulated energy depositions within the Ge crystal into individual strip data of the same form produced by the detector.

The geometrical model of the imager includes many of the internal components of the GeGI™ that are located near the crystal, since these materials have the potential to scatter radiation in a non-uniform way, creating a spatial gradient on the detector that may affect coded-aperture images. The model of the GeGI™ with the coded-aperture mask can be seen in Figure 11 and some of the internal components can be seen in Figure 12.

The response of the detector to energy-dependent gamma-ray radiation consists of an empirical, parametrized model of the strip response to energy depositions within the crystal. The model attempts to reproduce the photopeak widths, variations in efficiency as a function of distance from the boundaries of strips, and the position resolution of the events. Once the response model is applied to simulated data to predict the strip response of the detector, the processing cuts that are applied to the experimental data to select the single site events that are used for coded-aperture imaging are applied to the simulated data. Examples of detector hit maps for a measured and simulated ^{133}Ba source are shown in Figures 13 and 14, where the efficiency variations due to the 16 x 16 cross-strip pattern can be

seen. The units on the X and Y axes are in millimeters and the yellow regions of the plot represent high efficiencies, while the blue regions represent lower efficiency.

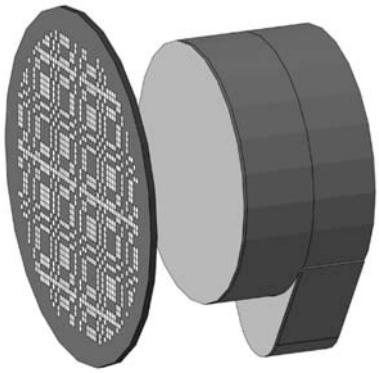

Figure 11. GEANT4 Model of GeGI™-5 with coded aperture mask

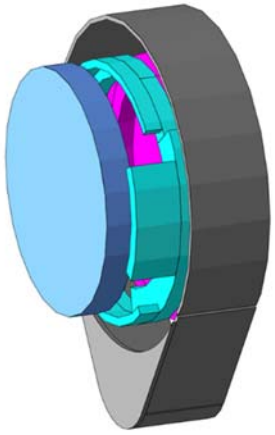

Figure 12. GEANT4 Model of GeGI™-5 with front cap removed

Using the response model for the detector, the imaging efficiencies can be calculated as a function of incident gamma-ray energy, source position in the field of view, and the mask-to-detector distance. To date, the effort has been on determining efficiencies using the analysis cuts used to select single-site events in the coded-aperture context, but there are plans to extend the model to accurately model multi-site events as well in order to evaluate the systematics in Compton imaging. Using simulated data to obtain these efficiencies allows the full range of the parameter space to be covered in a way that would be prohibitively difficult to do via measurements. These imaging efficiencies will be used as input to quantitative solvers, such as the DREAM code, to produce more accurate quantification of source activities.

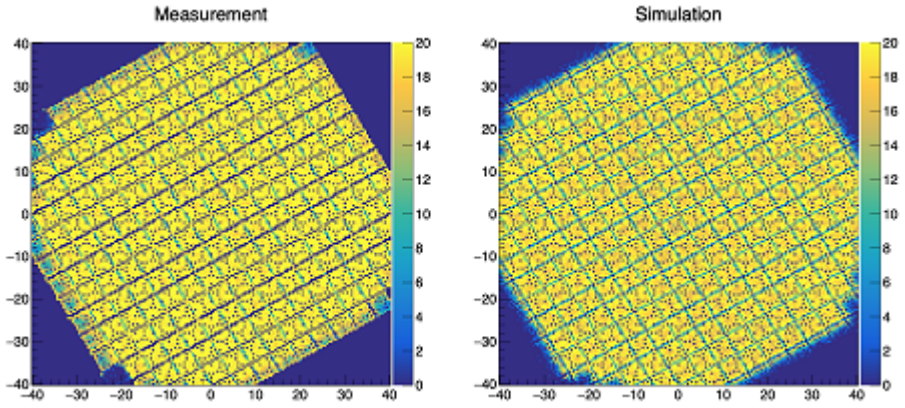

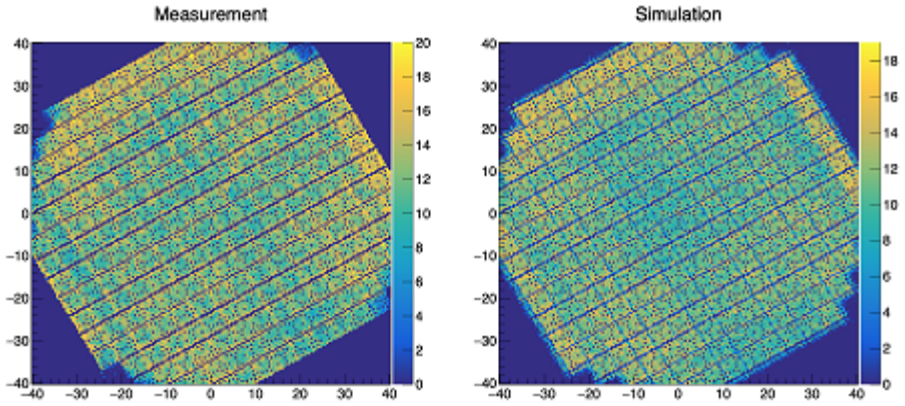

Figure 13 (upper) and Figure 14 (lower). Measured and simulated detector "hit" maps for single site events for 75 < E < 85 keV (upper) and 350 < E < 360 keV (lower) for a ^{133}Ba source. The axes are in millimeters.

4. Application of DREAM - A Markov Chain Monte Carlo Transport Method

While imaging can provide visual information and help define the shape and size of an object, the critical component of any holdup campaign is to quantify the mass of ^{235}U. The holdup problem can be cast as an inverse transport problem in which unknown source parameters are determined by using measured data. In the absence of explicit analytical solutions, which are only possible for a very small subset of scenarios, inverse problems are solved using what are known as implicit methods. Implicit methods make repeated postulations of the values of the unknown source parameters with the goal of iteratively improving the guesses and minimizing the difference between calculated and measured values.

A common stochastic approach is to cast the inverse problem in a Bayesian framework and use the Markov chain Monte Carlo (MCMC) approach to develop probability density functions that represent the uncertainty in the reconstructed source parameters.

DREAM[11], an advanced MCMC method used for optimization and uncertainty analysis, is used to characterize the holdup item using the measured data generated by the GeGI™. We first used GeGI imaging data in [Bledsoe et al, 2018], where source strength per energy line was determined for a small (approximately point) source. The imaged GeGI™ data contains a gamma-ray spectrum with statistical uncertainty for each pixel. DREAM uses this spectral information to determine source thickness and/or source strength while also propagating uncertainty from the measured data to the solution. Markov chain Monte Carlo simulations provide a generalized methodology for obtaining the posterior distribution of the unknown parameters in an inverse transport problem. This posterior distribution, $p(\mathbf{u}|M_o)$, represents the probability of a model $\mathbf{u}$ (where $\mathbf{u}$ is a vector representing postulated values for the unknown parameters), given observed measurements M_o. This distribution is proportional to a likelihood function times a prior probability distribution. The likelihood function is defined as:

$$p(M_o|\mathbf{u}) = \exp\left[-\frac{1}{2}\sum_{n=1}^{N}\sum_{d=1}^{D}\left(\frac{M_{n,d}(u_n)-M_{n,d,o}}{\sigma_{n,d}}\right)^2\right] \quad (1)$$

In equation (1), N is the total number of image pixels, *D* is the number of gamma-ray lines measured in each pixel (assumed to be the same for all pixels), $M_{n,d}(u_n)$ is the calculated response for line d in pixel n for the parameter u_n, $M_{n,d,o}$ is the observed measurement for line d in pixel n, and $\sigma_{n,d}$ is the uncertainty in the measurement line d in pixel n. $\mathbf{u}$ is the set of parameter values in all the pixels (u_n is the parameter value per pixel). The goal of the inverse problem is to find the regions for which $p(M_o|\mathbf{u})$ is at or near its maximum. The posterior distribution $p(\mathbf{u}|M_o)$ is a representation of the uncertainty in the solution given the uncertainty in the input data.

Note that the term inside the exponential is in the form of a χ^2 metric.

$$\chi^2 = \sum_{n=1}^{N} \sum_{d=1}^{D} \left(\frac{M_{n,d}(u_n) - M_{n,d,o}}{\sigma_{n,d}} \right)^2 \tag{2}$$

We can determine the reduced χ^2 metric (χ^2 per degree of freedom) to determine the goodness of fit of the postulated models determined by DREAM.

As we previously discussed in [Bledsoe et al, 2018], DREAM was chosen to overcome the limitations of traditional MCMC. In the traditional MCMC approaches, a single Markov chain is used. The chain begins at some random initial parameter set $\mathbf{u}_t$ [for which $p(\mathbf{u}_t|M_o)$ is calculated], and then a trial parameter set, $\mathbf{u}_{t+1}$, is created. The posterior distribution $p(\mathbf{u}_{t+1}|M_o)$ is calculated for this trial parameter set, and the trial set is either accepted or rejected according to the Metropolis acceptance probability:

$$\alpha(\mathbf{u}_t, \mathbf{u}_{t+1}) = \min\left[\frac{p(\mathbf{u}_t|M_o)}{p(\mathbf{u}_{t+1}|M_o)}, 1 \right]. \tag{3}$$

According to Eq. (2), if the trial point has a posterior smaller than the current chain state (i.e., parameters $\mathbf{u}_{t+1}$ yield a closer match between calculated and observed measurements), then the acceptance probability is 1, and the chain is moved to the trial state. If parameters $\mathbf{u}_{t+1}$ do not lead to a closer match between calculated and observed measurements, they may still be accepted. The probability of acceptance is equal to $p(\mathbf{u}_t|M_o)/p(\mathbf{u}_{t+1}|M_o)$. The chain progresses in this way until it creates the full posterior distribution describing the probabilities for the values of the unknown parameters.

The issue of choosing trial parameters has been explored for many years because the efficiency and speed of the algorithm depends heavily on it. Traditional MCMC approaches have generally been inefficient because trial parameters are either too close to the current point, leading to a high acceptance rate but slow convergence to the posterior distribution, or they are too far from the current point, leading to a low acceptance rate. The DREAM algorithm has been particularly successful at finding appropriate trial parameters and will be used throughout this work. DREAM (see reference 12, Bikowski et al 2010 for full description of the method) has been shown to greatly increase the speed of the MCMC process and to be highly successful for solving difficult optimization problems in the presence of noise[12]. It operates simultaneous Markov chains (typically 3–5) and uses the differential evolution[13] algorithm to generate trial points for each chain. In the case of multiple chains, the Metropolis ratio [Eq. (2)] becomes

$$\alpha(\mathbf{u}_1, \ldots, \mathbf{u}_N; \mathbf{u}_{1,trial}, \ldots, \mathbf{u}_{N,trial}) = \min\left[\frac{p(\mathbf{u}_1|M_o) + \cdots + p(\mathbf{u}_N|M_o)}{p(\mathbf{u}_{1,trial}|M_o) + \cdots + p(\mathbf{u}_{N,trial}|M_o)}, 1\right]. \quad (4)$$

In this work, a ray-tracing model[13] was used to calculate the flux per pixel per energy peak for each postulated parameter set $\mathbf{u}$. These fluxes were multiplied by energy-depended intrinsic efficiency values that were calculated by GEANT and by an energy-dependent correction factor representing the fraction of gamma rays that penetrate through closed mask elements.

4.1 Coded-Aperture Imaging and the Transport Model

Figure 15 presents a simple qualitative illustration of coded-aperture imaging. The image plane which contains the source being imaged, is partitioned into pixels. The signal emitted by these pixels passes through an aperture mask before reaching the detector array. The mask encodes the signals in such a way that the gamma spectrum emitted from each image pixel can be identified. These spectral data, represented by the term $M_{n,d}$ in Eq. (1), are what we use to determine the source parameters.

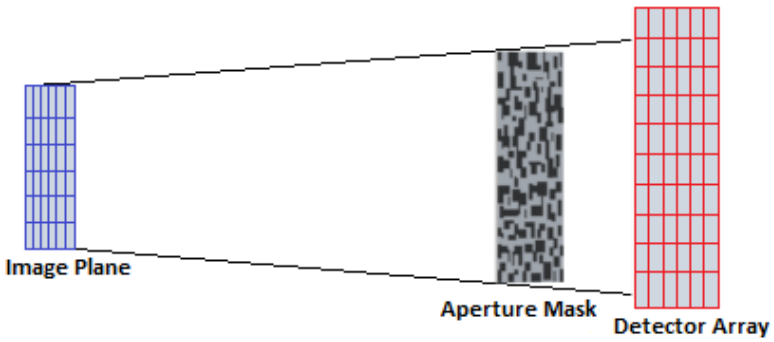

Figure 15. A highly simplified illustration of a coded-aperture system (taken from Ref 5 [Bledsoe et al, 2018].

For each postulated model $\mathbf{u}$, the spectrum in each source pixel $[M_{n,d}(u_n)]$ is calculated using a ray-tracing routine. A ray is traced from the center of each pixel in the image plane to the detector array. Using the process outlined in reference 14 [Favorite, Bledsoe, and Ketcheson, 2009], the number of photons impinging on the detector along the ray is calculated. The single-ray results are then multiplied by the pixel cross-sectional areas to approximate the total photons per second at the detector array due to the postulated source in each pixel. The energy line impingent on the detector array is multiplied by a geometric efficiency and a detector intrinsic efficiency factor that was determined by a previous calibration of the GeGI™. These results are multiplied by an aperture mask efficiency term, which accounts for the percentage of gamma-rays that penetrate through the closed

portions of the coded-aperture mask, and a heuristic spread function that accounts for the scattering of gamma rays in the detector crystal. The result of these calculations is a source intensity per energy line for each pixel in the image plane. The ray-tracing approach for calculating the flux was chosen because of its light computational burden, which allows for a rapid sampling of the thousands of postulated parameter sets $\mathbf{u}$. It introduces several simplifying assumptions, including that the source is uniform throughout a given pixel and that scattering into gamma-ray lines can be neglected. The impact of these assumptions is an area of current study.

5. Results and Discussion

The development and testing of the computational methods are on-going. Preliminary results are given for the quantitative estimate of ^{235}U mass.

5.1 Compton Imaging Results

Results for card ID#10 both bare and in an L-Duct are shown in Table 1, and were obtained using version 3.19.4.1199 of the vendor software in the "Analysis View" section of the Compton imaging mode. Once the spatial region was identified in the image, a rectangle was drawn about the area, enclosing a Region of Interest, which provides a subset of counts occurring within that region to contribute to the mass estimation functionality for the gamma lines selected. The uranium compound, namely U_3O_8, the density of the source material (0.68 g/cm^3), and the thickness of the absorber were input into the vendor software. The masses reported are based individually upon the intensity of the specific gamma energies, where a perfect combination of thicknesses and densities would result in each gamma-specific mass estimate having a very similar result with others from the same isotope.

Table 1: Compton Imaging Results

	Card ID#10 Bare			Card ID#10 L-Duct		
Gamma Energy (keV)	Counts	Radioactive Mass (g)	Mass Uncertainty (+/- g)	Counts	Radioactive Mass (g)	Mass Uncertainty (+/- g)
185.7	203209	10.59	0.0235	158978	10.58	0.0265
163.4	21066	10.47	0.0721	16346	10.72	0.0838
205.3	12517	8.53	0.0763	10620	9.12	0.0885
192.9	2133	10.74	0.23	1635	10.59	0.2600

Mass of a given area is calculated from the distance and the cosine of the angles to the points in the field of view, multiplied by the estimated thickness and density of the material. Uncertainties in these parameters do lead to swings in the resulting mass estimation, where another issue arises from the limitation of the angular resolution inherent to Compton imaging as an important area for optimization.

The weighted average mass of ^{235}U was (10.42 ± 0.02) g for the bare card, and (10.48 ± 0.02) g for the card inside the L-Duct. The deviation from the known mass of 11.16 g is -7.1% and -6.5% for the bare card and the card inside the L-Duct, respectively. We are working to improve performance accuracy which is not currently dominated by statistical uncertainties.

Maximum Likelihood Estimation (MLE) has been one of many image enhancement algorithms applied in Compton Imaging, where the overall goal is to minimize the spatial spreading associated with image reconstruction. A reduction in the spatial region is rather important for measurement locations where background comprises the isotope of interest that would add noise to the measurement in the form of larger spatial distribution. A current effort is underway to utilize paired Compton events to build a MLE-based image filter to improve spatial resolution, where data acquired can be compared directly with existing algorithms.

5.2 Quantification results using GeGI™ Coded Aperture Imaging and DREAM Method

The DREAM method was used with the coded-aperture data to determine the ^{235}U mass of card source #10 based on the bare source measurement (Figure 16). In this measurement, the card was 106.5 cm from the aperture mask and the mask was 7.1 cm from the GeGI, resulting in a total source-to-detector distance of 113.6 cm. The GeGI measured the card for 15 hours. An 18 × 22 subset of pixels encompassing the card was used in the DREAM analysis. This subset is shown in Figure 13. Statistical uncertainty per pixel ranged from 3% for pixels in the source "hotspots" (red pixels in Figure 13) to ~100% for pixels at the edge of the card.

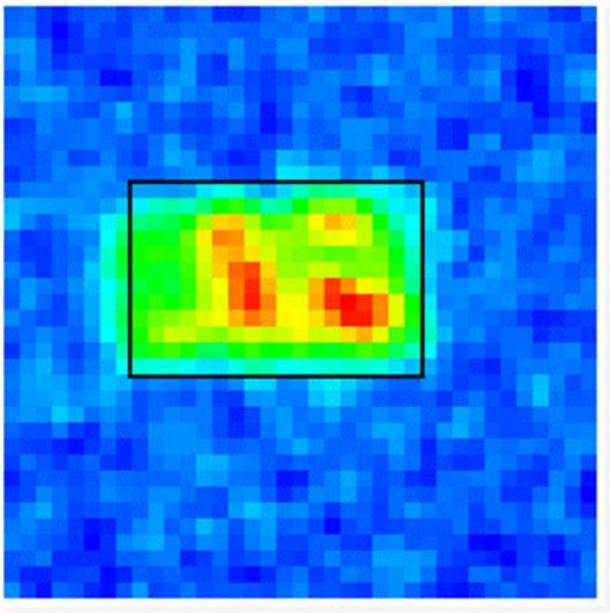

Figure 16. The GeGI™ image of the unshielded card source #10. The pixels inside the black box were used in the DREAM analysis.

Total peak counts for the 143 keV, 163 keV, 186 keV, and 205 keV lines were extracted from the GeGI data for each pixel. Using this as the measured data, The ^{235}U mass was then calculated per pixel, and the pixelated data was then combined (accounting for correlations between pixels) to determine the total ^{235}U mass and its uncertainty.

The χ^2 value for the first postulated model in the first iteration of DREAM was over 1×10^7 per degree of freedom. In 10,000 generations (run time: 14.3 seconds) this was reduced to 0.96 per degree of freedom, indicating a good match between calculated and measured values.

Using data from the four measured lines, the total ^{235}U mass for card was determined to be 11.11 ± 0.11 g. The listed ^{235}U mass of the card, 11.16 g, is within the 1σ estimate. The 1σ estimate would increase if other sources of uncertainty, such as modeling simplifications, were included in the DREAM analysis. Inclusion of other sources of uncertainty is an area of current research.

In a second analysis, the four energy lines were used separately to determine the mass. Results of this analysis are shown in Table 1. For The two lower energy lines DREAM underestimate the mass. The mass is calculated to with 1.2% of the actual value using the 186 keV line, but is overestimated for the 205 keV line. This lack of consistency indicates that improvements may be needed in our transport model.

Table 2. Calculated uranium mass for source card 10 using different measured values.

Measured Energy Lines	Calculated Mass (g)	Percent Difference from Actual Mass
144 keV	9.74 ± 0.36	-14.58%
163 keV	10.56 ± 0.40	-5.68%
186 keV	11.29 ± 0.13	1.15%
205 keV	12.43 ± 0.71	10.21%

6. Conclusions

The Compton imaging mode, with its limited spatial resolution, produces images with wide spatial distribution that provides an imperfect view of holdup distribution; however, data acquired for only 1 hour were able to identify the spatial regions with a level of satisfaction that may be sufficient for some usage scenarios as a means to help direct other methods such as ISOCS[15] or GGH. We note that the HEU measurements do not include the higher-energy lines, where the Compton resolution is better and will be an important adjunct to the lower-energy coded-aperture results. The Compton mass estimates deviate from the known mass of 11.16 g is -7.1% and -6.5% for the bare and the card inside the L-Duct, respectively. While these results are acceptable, it must be noted that the known value of uranium density was used. The power of the maximum likelihood algorithm that is being developed is in determining the optimal source characteristics when the source parameters are not known well.

Measurement data from GeGI^{TM} with the coded-aperture mask, combined with intrinsic efficiencies from GEANT4 model of the detector, and the DREAM MCMC transport method to correct for the attenuation characteristics and source-to-detector geometry, were used to solve for the mass of ^{235}U in the uranium card source. The deviation from the measured ^{235}U mass to the known mass was -1.2%

The preliminary work reported here show great promise. LEU holdup is a challenging problem but as we have shown considerable advances have been made in both instrumentation and data analysis, including the potential for quantitative imagery. More measurements and analyses are planned and will be reported elsewhere. A particular emphasis is in understanding the sources of uncertainty that ought to be propagated within the DREAM analysis.

7. Acknowledgement

The authors are grateful for the support of this project by the United States Department of Energy (U.S. DOE) National Nuclear Security Administration (NNSA) Office of Defense Nuclear Nonproliferation Research and Development.

The authors thank PHDs Inc., for providing the details of the GeGI^{TM} detector and its enclosure. This helped in the development of an accurate model of the detector using the GEANT4 code.

8. References

1. P. A. Russo, H. A. Smith, J. K. Sprinkle, Jr., C. W. Bjork, G. A. Sheppard, and S. E. Smith, "Evaluation of an Integrated Holdup Measurement System Using the GGH Formalism with the M3CA," Los Alamos National, Laboratory document LA-UR-95-3321.
2. P. A. Russo, T. R. Wenz, S. E. Smith and J. F. Harris, "Achieving Higher Accuracy in the Gamma-Ray, Spectroscopic Assay of Holdup," Los Alamos National Laboratory report LA-13699-MS (2000).
3. S. Agostinelli et al., "GEANT4 - a simulation toolkit", Nucl. Instr. Meth. A, vol. 506, no. 3, pp. 250-303, 2003.
4. K. C. Bledsoe, J. A. Favorite and T. Aldemir, "Application of the Differential Evolution Method to Solving Inverse Transport Problems," Nuclear Science and Engineering, 169(2):208-221, 2011. DOI: 10.13182/NSE10-28.
5. K. C. Bledsoe, J. A. Favorite, J. P. Lefebvre, R. A. Lefebvre, and M. A. Jessee, "Application of the DiffeRential Evolution Adaptive Metropolis (DREAM) Method for Uncertainty Quantification in Inverse Transport Problems," Transaction of the American Nuclear Society, 111, 743-746, 2014.
6. K. C. Bledsoe, M. A. Jessee, M. A. Blackstone, J. Knowles, K. P. Ziock, and J. P. Lefebvre, "Application of Markov Chain Monte Carlo for Uncertainty Quantification in Quantitative Imaging Problems," M&C 2019 – International Conference on Mathematics and Computational Methods Applied to Nuclear Science and Engineering, Portland, OR, August 25-29, 2018.
7. E.E. Fenimore, and T.M. Canon, Applied Optics 17 (1978) 337.
8. G.W. Phillips, "Gamma-ray imaging with Compton cameras", Nucl. Instr. Meth., B99 (1995) 674, and references therein.
9. R. Gottesman, E.E. Fenimore, App. Opt., vol 28, 4344-4352, 1989.
10. K.P. Ziock, M.A. Blackstone, Nucl. Inst. Meth. A, Vol. 916, 56, 2019.
11. J. A. Vrugt, et al., "Accelerating Markov chain Monte Carlo simulation by differential evolution with self-adaptive randomized subspace sampling," Int. J. Nonlin. Sci., 10(3), 237-290 (2009).

12. Bikowski, J. van der Kruk, J. A. Huisman, H. Vereecken, and J. A. Vrugt, “Inversion and Sensitivity Analysis of GPR Data with Waveguide Dispersion Using Markov Chain Monte Carlo Simulation,” Proceedings of the XIII International Conference on Ground Penetrating Radar, 1–5, June 21–25, 2010, Leece, Italy (2010).

13. R. Storn and K. Price, “Differential Evolution: A Simple and Efficient Heuristic for Global Optimization Over Continuous Spaces,” *J. Global Optim.*, **11**, 341–359 (1996).
14. J. A. Favorite, K. C. Bledsoe, and D. I. Ketcheson, “Surface and Volume Integrals of Uncollided Adjoint Fluxes and Forward-Adjoint Flux Products,” *Nucl. Sci. Eng*., **163**, 73-84 (2009).
15. R. Venkataraman, F, Bronson, V. Atrashkevich, B. Young, and M. Field, “Validation of In Situ Object Counting System (ISOCS) mathematical efficiency calibration software”. Nucl. Instrum. Mett. Phys Res, Sect. A 442, 450-454, 1999.